Silk fibroin based magnetic nanocomposites for actuator applications

Ander Reizabal, Carlos M. Costa*, Nelson Pereira, Leyre Pérez-Álvarez, Jose-Luis Vilas-Vilela and Senentxu Lanceros-Méndez*

A. Reizabal, Prof. Leyre Perez, Prof. Jose L. Vilas
BCMaterials, Basque Center for Materials, Applications and Nanostructures, UPV/EHU
Science Park, 48940 Leioa, Spain
Departamento de Química Física, Facultad de Ciencia Y Tecnología, Universidad del País
Vasco/EHU, Apdo. 644, Bilbao, Spain

Dr. C. M. Costa and N. Pereira
Centro de Física, Universidade do Minho, 4710-057 Braga, Portugal
E-mail: cmscosta@fisica.uminho.pt

Dr. C. M. Costa
Centro de Química, Universidade do Minho, 4710-057 Braga, Portugal

N. Pereira
Centro ALGORITMI, University of Minho, Campus de Azurém, 4800-058 Guimarães,
Portugal

Prof. S. Lanceros-Méndez
BCMaterials, Basque Center for Materials, Applications and Nanostructures
UPV/EHU Science Park
48940 Leioa, Spain
Email: senentxu.lanceros@bcmaterials.net

IKERBASQUE, Basque Foundation for Science
Bilbao
48013, Spain

Keywords: silk fibroin, magnetic nanoparticles, nanocomposite, magnetic actuator, smart and multifunctional materials

The need for technologies based environmentally friendlier materials, able to minimize the

global dependence on fossil fuel derivatives, promotes the development of new hybrid materials

based on natural polymers, such as silk derivatives. This work reports on a new generation of

magnetically active materials based on silk fibroin (SF) from *Bombyx mori* silkworm. Magnetic

cobalt ferrite (CFO) nanoparticles were introduced in an SF polymer matrix to develop SF/CFO

nanocomposites with filler contents of up to 20 wt%. It is shown that the inclusion of CFO

nanoparticles affects the β-sheet conformation of SF polymer having relevant effect on

1

mechanical and thermal properties. The incorporation of conductive nanoparticles into non-conductive matrix, induces an increase of electric conductivity and also on dielectric constant. The primitive magnetic behavior of CFO nanoparticles is successfully maintained after their incorporation into SF which has made possible the processing of magnetic SF. These results enabled the design and fabrication of a fully functional magnetic actuator based on SF, proving the suitable natural polymer based magnetic materials for a new generation of environmental friendlier smart and multifunctional materials.

1. Introduction

Recent technological and environmental advances are being redirected to develop technologies based on advanced materials that are not dependent on fossil fuels and/or critical elements [1]. Among them, smart materials showing piezoelectric [2], piezoresistive [3], photosensitive [4] or magnetics properties [5], among others, are particularly interesting for applications such as electronics, sensors or actuators. Polymer composites stand out in the development of smart and multifunctional materials as polymer matrixes in which suitable fillers, i,e, metallic, ceramic or magnetic micro/nanoparticles, are incorporated, in order to tailor materials response towards specific applications [6]. Further, those composites are often compatible with additive manufacturing technologies that enlarges their applicability.

Different synthetic polymer matrices are being used in the development of polymer composites such as thermoplastics, thermosets or elastomers, but to reduce the processing and consumption of fossil fuels, biopolymers are increasingly being used [7].

Silk fibroin polymer (SF) has been investigated for biomedical [8], energy storage [9] and electronic applications [10] due to its excellent intrinsic characteristics.

SF is a natural macromolecular protein produced in the specialized glades of Bombyx Mori silkworm [11]. SF is packed in cocoons and acts as shield versus foreign threats, solar radiation, temperature, humidity, parasites and predators during the metamorphosis process of worms [12].

Derived from this natural purpose, SF presents biodegradability [13], high tensile strength [13], good elasticity, and excellent resilience [14]. Silk fibers are among the strongest and toughest materials obtainable from nature [15], indeed, they have shown to be five to six times lighter than steel while having a similar strength [16] and being tougher than all existing synthetic fibers, including high-performance polyethylene or Kevlar [17]. In addition, silk shows good flexibility, optical transparency, thermal stability, ultra-thinness and ultra-smoothness. Further, it is abundant in nature and shows the possibility to tune the aforementioned properties to specific application requirements [18]. Taking advantage of these promising characteristics, silk is positioned as one of the most interesting materials in the global transition towards production and use of natural friendly materials.

Accordingly, some works have been focused on combining both materials in order to improve the SF applicability, and approach to smart functional materials based on natural materials. In order to obtain piezoresistive sensors, SF was successfully combined with carbon nanotubes [10] and applied as pressures sensor. Ionic liquids were also employed as additives giving to the SF the ability to respond to external electric fields in order to form an electric actuator [19]. In this context, magnetic fiber composites based on silk fibroin (SF) with cobalt ferrite ($CoFe_2O_4$) or magnetite (Fe_3O_4) nanoparticles were fabricated as scaffolds for tissue engineering applications by electrospinning [20], showing that neither SF pristine fibers nor the SF composites are cytotoxic, indicating their suitability for tissue engineering applications [20].

Further, nanocomposites based on silk fibroin (SF) and superparamagnetic iron oxide nanoparticles (SPIONs) have been also fabricated by electrospinning as a magnetically responsive cytocompatible scaffold for tissue engineering [21]. Related magnetic silk fibroin protein scaffolds integrating magnetic materials have shown excellent hyperthermia properties, not toxicity to osteogenic cells and improved cell adhesion and proliferation [22].

Silk fibroin nanoparticles were investigated for drug release in which these nanoparticles were modified with bovine serum albumin and magnetic nanoparticles in order to improve the encapsulation of the drug [23].

Magnetic silk fibroin e-gel scaffolds prepared by the electrogelation process of concentrated *Bombyx mori* silk fibroin aqueous solution showed an improved effect on cell viability [24].

Finally, magnetic nanoparticles have been added to related materials such as silk-elastin-like protein polymers (SELPs) also for biomedical applications [25]. In addition, silk fibroin (SF) nanofibers have been used as template and coating to synthesize nanoparticles of core-shell (Fe_3O_4) / SF magnetite with controllable size [26].

Thus, magnetic nanocomposites based on silk fibroin have been traditionally investigated for biomedical applications. Taking into consideration its excellent mechanical and the ability to develop magnetic composites, the present work demonstrates the development of silk fibroin nanocomposites with cobalt ferrite nanoparticles for electronica purposes, showing further their applicability as magnetic actuator. The effects of cobalt ferrite nanoparticles concentration on the morphological, thermal, mechanical, electrical and magnetic properties of silk fibroin composites have been analyzed, showing that it is possible obtain magnetic sensors and actuators based on prepared silk derivatives.

2. Results and discussion

2.1. Nanocomposites morphology and filler dispersion

Homogeneous dispersion of the fillers along the polymer matrix will provide a homogeneous behaviour across the nanocomposites. Thus, an important issue in the development of nanocomposite materials is the promotion of a suitable dispersion of fillers within the polymer matrix. In order to analyse CFO nanoparticles dispersion, optical images, SEM and EDX were used. Representative images from these three complementary techniques are shown in **Figure 1**. Optical photographs (Figure 1a) reveal a macroscopic homogeneous dispersion of the CFO

WILEY-VCH

nanoparticles for filler concentrations below 5 wt%. However, due to magnetic nanoparticles aggregation trend [27], CFO nanoparticles form macroscopic clusters for filler concentrations above 5 wt%. Magnetic nanoparticles show a tendency to aggregate due long-range magnetic and van der Waals attractive forces [28]. This aggregation process can be divided into two main steps; a first one where Brownian motion leads the dispersed nanoparticles to come together in discrete μ-sized agglomerates; and a second step where collision and consequent adhesion effects make the μ-sized agglomerates to join into higher clusters [27, 29]. Amplifications of the optical images reveal that up to 5wt% of CFO content, nanoparticles are mainly affected by the first agglomeration regime, forming a well dispersed micro sized clusters. Above 5wt% CFO concentration, the volume occupied by nanoparticles grow and consequently, the collision and adhesion effects between micro sized clusters increase, resulting in the formation of macroscopic clusters.

SEM and EDX (for Fe and Co) images are shown in Figure 1b revealing the nanofiller dispersion along the nanocomposites surface. Both SEM and EDX images reveal that increasing filler content from 5 wt% to 20 wt% results in increasing nanoparticle clustering, specially at the outer side of the samples. On the other hand, both SEM images and, in particular, EDX results (Fe and Co signal, represented as blue and red dots) show that the nanoparticles are homogenously dispersed along the nanocomposites thickness, showing that even when nanoparticles clustering is macroscopically observable on the nanocomposites surface, the CFO nanoparticles are overall properly dispersed through the nanocomposites.

2.2. Vibrational FTIR-ATR spectra

Figure 2 shows the FTIR spectra and the vibrational band assignments of the main molecular conformations for the CFO/SF nanocomposites. The full-range FTIR spectra of the samples in the frequency range from 4000 to 600 cm^{-1} are represented in Figure 2a. It is observed that no peaks are formed or displaced after CFO nanoparticles addition, and all the samples show the main representative Amide I, II, OH stretching vibration, H-bond and NH stretching vibration peaks of SF [30] at 1600-1700, 1517-1539, 3500-3000, cm^{-1} respectively (Table 1). Thus, it is shown that magnetic nanoparticles addition does not induce any changes in the primary SF structure.

Physical-chemical properties of the SF films are highly influenced by the secondary structure of polypeptide chains, which was analyzed from the measured area under the deconvoluted peaks of amide I (Figure 2b). The observed main representative vibration peaks of the different secondary structures used for the Amide I deconvolution (side chains (SC), β-sheets (B), random coil (RC), α-helix (A) and turns (T)) are listed in Table 1. It is observed that the nanocomposites processing results in a highly crystalized SF, mainly dominated by β-sheet structures in all the cases. The incorporation of CFO nanoparticles progressively leads to a decrease of the β-sheet conformation content. Consequently, β-sheet portion ranges from 50% in neat SF to values around 40% in samples with 20 wt% CFO. This fact confirms previous studies that suggest that the inclusion of CFO fillers hinder the formation of β-sheet crystals [20].

2.3. Thermal and dynamic mechanical analysis.

Thermal degradation and thermal transitions define the thermal range in which materials can be applied, allowing also the understanding of the physico-chemical properties of the composites. Thermogravimetric curves (TGA) and differential scanning calorimetry (DSC) were used (**Figure 3a and 3b**, respectively) for the thermal characterization of the samples. TGA and the corresponding derivates (DTGA) show (Figure 3a) that neat SF films present an initial weight loss of 6% at 100 $^{\circ}$C which corresponds with solvent loss (water + formic acid). A second weight loss, observed at 290 $^{\circ}$C, is mainly ascribed to the breakdown of SF side chain groups, amino acid residues and the split of peptide bonds [33]. The final weight loss at 650 $^{\circ}$C matches with organic polypeptide chains combustion. With the inclusion of the CFO magnetic nanoparticles to the SF matrix, the solvent loss signal remains still visible at 100 $^{\circ}$C. Similarly, no observable changes happen in the second degradation step. The final weight loss (signaled by a black arrow), on the contrary, switches to lower temperatures as CFO nanoparticles are added, effect which is attributed to the decrease of the β-sheets structures (observed in FTIR data, Figure 2b), which are the main responsible of SF thermal stability [34]. As a result, the final degradation temperature of the CFO/SF nanocomposites moves from 580°C in the sample with 0.5 wt% CFO content to 500 $^{\circ}$C in the sample with 20 wt% CFO content. The remaining residues after final organic phase combustion correspond with the non-organic content of the CFO nanoparticles [35]. Thus, the final residues increase with increasing filler content from 0.4% in the sample with 0.5 wt% CFO content to 8% in the sample with 20 wt% CFO content.

SF and CFO/SF nanocomposites thermal transitions were studied by DSC. Bonded solvent evaporation may mask the SF thermal transitions [19] and therefore, in order to remove them, all the samples were heated at 170 $^{\circ}$C for 5 minutes before the DSC analysis. The DSC thermograms after this procedure are plotted in figure 3b.

SF and CFO/SF nanocomposites show a clear endothermic peak at 290 ºC, corresponding to the breakdown of side chain groups, amino acid residues and the split of peptide bonds observed in TGA curves. At lower temperatures it is also observed a heat flow variation commonly

related with the glass transition temperature (signaled by a black arrow) [34a, 36]. This effect has been also reported in electrospun membranes with different CFO contents [20]. However, no significant differences could be observed as a consequence of the incorporation of CFO fillers. DMA was carried out in order to further clarify SF and CFO/SF nanocomposites thermal transitions and to evaluate the viscoelastic properties of the materials. The storage modulus (E´) obtained from DMA is plotted in Figure 3c showing, for all samples, that the storage modulus shows a first increase of E´ related to solvents evaporation. Due to the plasticizer effect of solvents, after their evaporation the polypeptide chain becomes stiffer and consequently E´ becomes three times larger. At higher temperatures, the behavior of SF and CFO/SF nanocomposites become different. It can be observed for neat SF films that E´ start decreasing shortly after reaching 125 ℃ (signaled by a right-facing black arrow) due to molecular chains flowing process (glass transition). Further, E´ continues decreasing with increasing temperature until a strong fall of its value is observed due to side chain groups breakdown and peptide bonds split. CFO/SF nanocomposites, on the contrary, maintain the glassy state stable until 160-175 ℃ where suddenly undergo the glass transition (signaled by a left-facing black arrow). After that, E´ also continues to decrease with increasing temperature until the rapid decrease is observed. Thus, CFP/SF nanocomposites behavior shows that CFO nanoparticles are filling the free volume and consequently increase the needed energy for the glass transition to occur. This behavior also explains the hindering effect of CFO fillers over β-sheet crystals formation observed in FTIR-ATR results.

2.4. Dielectric properties

CFO/SF nanocomposites dielectric behaviour was evaluated taking into consideration the equations 2, 3 and 4 presented in the experimental section. From these equations, the real (ε') and imaginary (ε'') components of the dielectric constant, as well as the a.c. electrical conductivity ($\sigma_{a.c}$), were obtained (**Figure 4**).

The dielectric behaviour of polymers is dependent on the contributions of dipolar moments, cations and space charge polarizations [37]. Neat SF is mainly free of cations and space charge polarization and, as a consequence, it shows ε' values around 2 (Figures 4a). The increase of polarising contributors derived from CFO nanoparticles addition, mostly dominated by interfacial and space charge polarization [38], induces the progressive increasing of ε' in the CFO/SF nanocomposites as shown in figure 4a) and 4b). In the different nanocomposites, increasing frequency leads to a decrease of ε' as consequence to the dipole relaxation process [39], due to the inability of the dipolar contributions to follow the increasing electric field variations [40]. Further, for CFO/SF nanocomposites, the decrease of ε' with increasing frequency is larger for the samples with the larger filler contents, indicating the slower dynamic of the interfacial contributions [37]. It is to notice that the increase of the dielectric response with increasing filler content is not linear (Figure 4b), being observed a strong increase of the dielectric response for filler contents up to 1%wt, and a progressive slow increase for larger filler contents. This effect reveals the important contributions to the dielectric response of defective structures and interfacial contributions, which becomes less relevant with nanofiller aggregation and hindered mobility [41].

In fact, as the main contributions to the dielectric response comes from interfacial and space charge contributions, this leads to an increase of the dielectric losses, ε'', (Figure 4b) and of the a.c. electrical conductivity (Figure 4c) with increasing filler content. It is to notice that the increase of the dielectric losses with increasing ferrite content (Figure 4b) is not linear due to particle agglomeration effects. As it is shown in Figure 4c, the addition of CFO nanoparticles

induces an increase on the a.c. which increases with increasing frequency, indicating the local contribution to the electrical conductivity [42].

2.5. Magnetic properties

In order to understand the magnetic behaviour of the CFO/SF nanocomposites, all samples were measured in a vibrating sample magnetometer (VSM) at room temperature in a temperature range from 20 to 175 ºC (**Figure 5**). The used nanoparticles with a size distribution around 50 nm, are larger than the critical size of 27-28 nm for single domain particles [43], so the magnetic behavior of the nanocomposites is expected to be dominated by a multi-domain magnetic behavior. Figure 5a, shows the hysteresis loops of neat CFO and CFO/SF nanocomposites, whereas Figure 5b shows the most important parameters obtained from the hysteresis loops.

Figure 5a shows that CFO nanoparticles present the typical hysteresis loop indicating the random orientation of magnetic domains. Under strong magnetic field (20 KOe), CFO nanoparticles reach the saturation (60 emu/g) signaling that all magnetic domains have been oriented in the direction of the field. When magnetic field is removed most domain loss the orientation, but few remains invariable conserving certain magnetization (30 emu/g), which is easily removed when a magnetic field of 1.97 kOe is applied in the opposite direction [44].

CFO/SF composites also reveal closed hysteresis loops showing that the magnetic particles preserve their original ferromagnetic behavior once included in the SF matrix [45]. It is also observed that the magnetic behavior of the nanocomposites is highly dependent on the CFO content. (Figure 5b). As expected, the magnetization saturation and magnetic field remanence increase with CFO particles addition. In nanocomposites, CFO nanoparticles are dispersed throughout the matrix and consequently their magnetic fields do not just add up, depending on different factors such as nanofiller agglomeration. The saturation and remanence magnetization decrease from 60 and 30 emu/g respectively in neat CFO nanoparticles to 7 and 4 emu/g in 20 wt% CFO.

10

The coercive field of the CFO/SF nanocomposites increases with in increasing fillers addition, until reaching a limit of 2.2 KOe at 10 wt% CFO where it begins to decrease. This behavior match with previously reported data on CFO nanoparticles size-coercivity dependence [46]. It was concluded that CFO magnetic nanoparticles coercivity increases with increasing size until reaching a nanoparticle size of 100 nm, where coercivity start decreasing again. Thus, it can be concluded that the agglomeration effect observed in SF/CFO nanocomposites (as discussed in the morphological analysis), leads to a similar effect of having increasingly larger particles, matching the CFO nanoparticles size in 10 wt% CFO with 100 nm.

The temperature dependence of the magnetic behavior of the nanocomposites is shown in Figure 5c. The 20 wt% CFO composite data is plotted as representative for all composites. As the Curie temperature of the CFO particles is 500 $^{\circ}$C [47], no changes in magnetic properties are observed in this sense in Figure 6c. Further, the applied maximum temperature (175 $^{\circ}$C) is near the SF glass transition previously determined between 160 and 175 $^{\circ}$C, thus, the thermal measurements will report data on nanocomposites mainly in the glassy state (below 175 $^{\circ}$C) and in the first rubbery points. Temperatures do not exceed T_g in any case, ensuring the SF mechanical stability.

Figure 5c shows that closed hysteresis loops are observed in all temperature range, confirming that SF/CFO nanocomposites still maintain the magnetic behavior even at high temperatures. As temperature increases, maximum magnetization, coercivity and remanence decrease (Figure 5d), as expected, due to the decrease in magneto-crystalline anisotropy [48]. Due to the temperature increase, nanoparticles internal energy increases, and the energy barrier that separates the energetically degenerated magnetic orientations decreases, thus a minor energy fluctuation lead to the switching of domains orientation. As a consequence of temperature increases, lower applied magnetic field is necessary to induce the maximum magnetization, lower amount of domains remains magnetized after magnetic field removal and consequently lower field is necessary to demagnetize the samples (Figure 5d) [46]. Thus, the addition of CFO

nanoparticles provides the CFO/SF composites with a tailorable magnetic response and opens a functional way to produce sensors and actuators with adjustable properties.

3. Magnetic actuator

Considering to the magnetic properties of the SF/CFO nanocomposites, a device that acts as magnetic actuator switch in the proximity of a magnetic field was fabricated. For that, a resistive ink based on carbon nanotubes was deposited over the SF/CFO nanocomposite film to act as conductor and placed in front of another conductive surface separated with an air gap of 500 µm as shown in **Figure 6a**). When no magnetic field is present, the conductive surfaces are mechanically separated from each other, being in open circuit. When a magnetic field is present the two conductive surfaces touch, and the resistance decreases as the circuit is closed, as it is shown in the schematic representation in Figure 6a).

The magnetic actuator was fabricated by placing the 20 wt% CFO composite (SF/CFO/Carbon) on a cantilever configuration with the carbon surface turn to the conductive structure fabricated by 3D printing with conductive PLA (CDP11720) from Proto-pasta using a PRUSA i3 MK3 as shown Figure 6a) (see video in supplementary information). The electronic circuit is based on a voltage divider and an ADC (Analog to digital converter) of 10 bits present on the Arduino Nano converts the voltage variation (resistance variation through equation 1), in the magnetic switch to a digital signal that then sends the data to the laptop via USB.

$$Rs = \frac{5 \times R1}{5 - V_{Rs}} \qquad (1)$$

When a magnetic field is present by approaching a permanent magnet (BX0C8-N52 from K&J Magnetics, Inc) with a surface field of approximately 5336 Gauss, the film bends and touches the conductive plate that changes the resistance of the circuit. Figure 6b) shows the resistance variation from open circuit to approximately 700 MΩ when the magnet is approximated.

It is observed that the resistance behavior is reproductively when the magnet is approximate to the nanocomposites as a function of the time (Figure 6b). As expected, if the sample is closer to the magnet, the displacement increases and the resistance decreases (see video in supplementary information).

Taking into account, the magnetic and dielectric response of the developed CFO/SF nanocomposites, this work demonstrates that it is possible to develop magnetically responsive actuators based on natural polymer such as silk fibroin in order to produce a new generation of environmentally friendly multifunctional materials.

4. Conclusion

CFO/SF nanocomposites were successfully processed by solvent casting. The selected SF solution in formic acid allowed the incorporation of CFO nanoparticles with different amount, ranging from 0.5 to 20 wt%. Good dispersion of the CFO nanoparticles is achieved, as observed by SEM and confirmed by EDX analysis. Formic acid makes the polypeptide structure to fold into a highly ordered structure rich in β-sheets, organization which provides to the samples with large thermal stability, being able to stand temperatures above 250 $^{\circ}$C without thermal degradation. The incorporation of the CFO nanoparticles in the SF matrix strongly affects nanocomposites behaviour given to the thermal and mechanical stability to the samples also above 160ºC. CFO nanoparticles incorporation, leads to a significant increase of samples dielectric response, reaching to values above 20 with when CFO contents of 20wt% are added to SF. Successfully, the CFO nanoparticles incorporation to the SF matrix results in a magnetic composite characterized by strong magnetic response, even with low CFO nanoparticles addition, SF/CFO nanocomposites show magnetization values around 10 emu/g and coercitive values of almost 4 kOe, when 20wt% of CFO nanoparticles are added. These magnetic behaviour of the nanocomposite allowed the development of magnetic actuators based on natural polymer.

5. Experimental section

5.1. Materials

Silk fibroin (SF) was extracted from Bombyx mori cocoons supplied by APPACDM from Castelo Branco (Portugal). Formic acid (FA), sodium carbonate (Na_2CO_3) and calcium chloride ($CaCl_2$) were purchased from Sigma-Aldrich. Cobalt ferrite (CFO) nanoparticles with 35-55 nm size were brought from Nanoamor.

5.2. Silk Fibroin extraction.

Silk fibroin extraction was performed as described in previous works [10]. After complete cleaning, silk cocoons were cut into small pieces and degummed by boiling in 0.05%wt. Na_2CO_3 water solution during 30 minutes. Fibers were then rinsed in distilled water for residual silk sericin removal and dried overnight. Clean silk fibroin was dissolved in a formic acid/$CaCl_2$ 0.17M solution in a liquid to silk ratio of 12:1 w/v (12 ml formic acid per gram of SF), and then centrifuged at 7,500 rpm during 10 minutes for the removal of non-dissolved residues. The obtained solution was casted overnight for solvent removing and finally immersed in distilled water bath for two days to remove the inner salts.

5.3. CFO/SF nanocomposites preparation

CFO/SF nanocomposites of 0.5, 1, 5, 10 and 20 wt. % of CFO were prepared by a mixing and solvent casting process, depicted in **Figure 7**. Before preparation of the nanocomposites, all the components were well dried in an oven at 40 °C for 24h. After that, two different solutions were prepared, a first one based on SF dissolved in FA (liquid to silk ratio of 5:1 w/v) and a second one with CFO nanoparticles dispersed in formic acid by ultrasonication (3 h.). Both solutions were mixed in a vortex mixer MX-S during 5 min and casted over polyethylene petri dishes for 24 hours. The obtained composites with a thickness of 40 μm were kept in dry atmosphere until their use. Neat SF films were prepared by the same method, without CFO nanoparticles incorporation.

5.4. Characterization techniques and procedures.

Scanning electron microscope (SEM) (SEM, NanoSEM - FEI Nova 200 (FEG/SEM)) and energy dispersive X-ray spectroscopy (EDX) (Hitachi Tabletop Microscope TM 3000) were used in order to study CFO/SF composites morphology, as well as nanoparticles dispersion and distribution within the films. Prior the measurements, SF/ CFO films were coated with a conductive 20 nm gold layer by sputtering with a Polaron SC502 apparatus.

Attenuated Total Reflectance (ATR)/Fourier Transform infrared (FTIR) measurements were performed with a Jasco FT/IR-4100 system apparatus at room temperature from 4000 to 600 cm^{-1} using 64 scans at a resolution of 4 cm^{-1}. The assignment of the vibrational bands was performed by deconvolution of the Amide I region, as described in previous works [19].

Thermal analysis was performed with a Thermal Gravimetric Analyzer (TGA) TGA/SDTA 851e Metter Toledo apparatus in the temperature range from 25 to 800 °C at a heating rate 10 °C min^{-1} under air flow. Differential scanning calorimetry (DSC) measurements were carried out with a Mettler Toledo DSC 822e equipment. In order to remove bonded water, nanocomposites were first heated from 25 to 170 °C and then cooled to 25 °C. Calorimetric scanning corresponds to the second heating process from 25 to 350 °C. All heating and cooling ramps were performed at 10 °C min^{-1} under nitrogen purge (50 mL min^{-1}).

The mechanical response of the nanocomposites to thermal variations was analyzed by dynamic mechanical analysis (DMA), with a Mettler Toledo DMA1 apparatus in tensile mode. Both storage modulus (E´) and loss tangent (tan δ_{DMA}) were measured as function of the temperature from 0 to 280 °C at 10 °C·min^{-1} at a frequency of 1 Hz.

In order to study samples dielectric response, the capacity (C) and dielectric losses (tan δ) of the CFO/SF composites was obtained using an automatic Quadteh 1929 Precision LCR meter at room temperature in the frequency range of 20 Hz to 1 MHz. Measurements were carried out in samples in which circular gold electrodes of 5 mm diameter were deposited on both sites of

each sample by magnetron sputtering with a Polaron Coater SC502. The real (ε') and imaginary (ε'') part of the dielectric function were calculated from equations 2 and 3 respectively:

$$\varepsilon' = \frac{C \cdot d}{\varepsilon_0 \cdot A} \qquad (2)$$

and

$$\varepsilon'' = \tan \delta \cdot \varepsilon' \qquad (3)$$

where C is the sample capacity, ε_0 is the permittivity of vacuum (8.85×10^{-12} F·m^{-1}), A is the electrode area and d is the films thickness.

Nanocomposites AC electrical conductivity (σ_{AC}) was calculated using equation 4:

$$\sigma_{AC} = \varepsilon_0 \omega \varepsilon'' \qquad (4)$$

Where ω is the angular frequency ($\omega = 2\pi\int$).

Nanocomposites magnetic properties were obtained with a MicroSense EZ7 vibrating sample magnetometer (VSM) from -1.8 to 1.8 T. The temperature dependent magnetic response of the CFO/SF 20% sample was studied at 50, 100, 150 and 175 °C.

Supporting Information
Representative video of SF/CFO based actuators.

Received: ((will be filled in by the editorial staff))
Revised: ((will be filled in by the editorial staff))
Published online: ((will be filled in by the editorial staff))

References

[1]   B. H. Fumes, M. R. Silva, F. N. Andrade, C. E. D. Nazario, F. M. Lanças, *TrAC, Trends Anal. Chem.* **2015**, *71*, 9-25.

[2]   M. Ferrari, V. Ferrari, M. Guizzetti, D. Marioli, in *Sensors and Microsystems: AISEM 2009 Proceedings* (Eds.: P. Malcovati, A. Baschirotto, A. d'Amico, C. Natale), Springer Netherlands, Dordrecht, **2010**, pp. 77-81.

[3]   B. F. Gonçalves, P. Costa, J. Oliveira, S. Ribeiro, V. Correia, G. Botelho, S. Lanceros-Mendez, *J. Polym. Sci., Part B: Polym. Phys.* **2016**, *54*, 2092-2103.

[4]   L. B. Sun Jing-Bo, Huang Xue-Guang,Cai Kun-Peng,Zhou Ji,Li Long-Tu, *J. Inorg. Mater.* **2009**, *24*, 1147-1150.

[5]   O. Reynet, A. L. Adenot, S. Deprot, O. Acher, M. Latrach, *Phys. Rev. B* **2002**, *66*, 094412.

[6]   aC. Mendes-Felipe, J. Oliveira, I. Etxebarria, J. L. Vilas-Vilela, S. Lanceros-Mendez, *Adv. Mater. Technol.* **2019**, *4*, 1800618; bJ. Oliveira, V. Correia, H. Castro, P. Martins, S. Lanceros-Mendez, *Addit. Manuf.* **2018**, *21*, 269-283.

17

[7]   P. Baishya, M. Mandal, P. Gogoi, T. K. Maji, *Handbook of Composites from Renewable Materials* **2017**, pp. 433-459.

[8]   Z. Xu, L. Shi, M. Yang, L. Zhu, *Mater. Sci. Eng., C* **2019**, *95*, 302-311.

[9]   R. F. P. Pereira, R. Brito-Pereira, R. Gonçalves, M. P. Silva, C. M. Costa, M. M. Silva, V. de Zea Bermudez, S. Lanceros-Méndez, *ACS Appl. Mater. Interfaces* **2018**, *10*, 5385-5394.

[10]   A. Reizabal, S. Gonçalves, R. Brito-Pereira, P. Costa, C. M. Costa, L. Pérez-Álvarez, J. L. Vilas-Vilela, S. Lanceros-Méndez, *Nanoscale Adv.* **2019**, *1*, 2284-2292.

[11]   H. F. Zhao, Y. Li, L. Z. Sha, *Preparation of functional air filter material based on biodegradable fibers and nano titanium dioxide, Vol. 13*, **2018**.

[12]   J. Kaur, R. Rajkhowa, T. Tsuzuki, K. Millington, J. Zhang, X. Wang, *Biomacromolecules* **2013**, *14*, 3660-3667.

[13]   H.-y. Cheung, M.-p. Ho, K.-t. Lau, F. Cardona, D. Hui, *Composites, Part B* **2009**, *40*, 655-663.

[14]   J. Pérez-Rigueiro, C. Viney, J. Llorca, M. Elices, *J. Appl. Polym. Sci.* **1998**, *70*, 2439-2447.

[15]   F. G. Omenetto, D. L. Kaplan, *Science* **2010**, *329*, 528-531.

[16]   L.-D. Koh, J. Yeo, Y. Y. Lee, Q. Ong, M. Han, B. C. K. Tee, *Mater. Sci. Eng., C* **2018**, *86*, 151-172.

[17]   J. M. Gosline, P. A. Guerette, C. S. Ortlepp, K. N. Savage, *J. Exp. Biol.* **1999**, *202*, 3295-3303.

[18]   aH. Wang, B. Zhu, H. Wang, X. Ma, Y. Hao, X. Chen, *Small* **2016**, *12*, 3360-3365; bC.-H. Wang, C.-Y. Hsieh, J.-C. Hwang, *Adv. Mater.* **2011**, *23*, 1630-1634; cJ. D. Larson, C. V. Fengel, N. P. Bradshaw, I. S. Romero, J. M. Leger, A. R. Murphy, *Mater. Chem. Phys.* **2017**, *186*, 67-74.

[19]   A. Reizabal, D. M. Correia, C. M. Costa, L. Perez-Alvarez, J. L. Vilas-Vilela, S. Lanceros-Méndez, *ACS Appl. Mater. Interfaces* **2019**, *11*, 30197-30206.

[20]   R. Brito-Pereira, D. M. Correia, C. Ribeiro, A. Francesko, I. Etxebarria, L. Pérez-Álvarez, J. L. Vilas, P. Martins, S. Lanceros-Mendez, *Composites, Part B* **2018**, *141*, 70-75.

[21]   Ö. Lalegül-Ülker, M. T. Vurat, A. E. Elçin, Y. M. Elçin, *J. Appl. Polym. Sci.* **2019**, *136*, 48040.

[22]   S. K. Samal, M. Dash, T. Shelyakova, H. A. Declercq, M. Uhlarz, M. Bañobre-López, P. Dubruel, M. Cornelissen, T. Herrmannsdörfer, J. Rivas, G. Padeletti, S. De Smedt, K. Braeckmans, D. L. Kaplan, V. A. Dediu, *ACS Appl. Mater. Interfaces* **2015**, *7*, 6282-6292.

[23]   J. L. Wilson, P. Poddar, N. A. Frey, H. Srikanth, K. Mohomed, J. P. Harmon, S. Kotha, J. Wachsmuth, *J. Appl. Phys.* **2004**, *95*, 1439-1443.

[24]   Z. Karahaliloğlu, E. Yalçın, M. Demirbilek, E. B. Denkbaş, *J. Bioact. Compat. Polym.* **2017**, *32*, 596-614.

[25]   M. M. Fernandes, D. M. Correia, A. da Costa, S. Ribeiro, M. Casal, S. Lanceros-Méndez, R. Machado, *Composites, Part B* **2018**, *153*, 413-419.

[26]   W. Sheng, J. Liu, S. Liu, Q. Lu, D. L. Kaplan, H. Zhu, *J. Mater. Chem. B* **2014**, *2*, 7394-7402.

[27]   T. Phenrat, N. Saleh, K. Sirk, R. D. Tilton, G. V. Lowry, *Environ. Sci. Technol.* **2007**, *41*, 284-290.

[28]   P. L. Golas, S. Louie, G. V. Lowry, K. Matyjaszewski, R. D. Tilton, *Langmuir* **2010**, *26*, 16890-16900.

[29]   S. P. Yeap, J. Lim, B. S. Ooi, A. L. Ahmad, *J. Nanopart. Res.* **2017**, *19*, 368.

[30]   J. Shao, J. Zheng, J. Liu, C. M. Carr, *J. Appl. Polym. Sci.* **2005**, *96*, 1999-2004.

[31]   aO. N. Tretinnikov, Y. Tamada, *Langmuir* **2001**, *17*, 7406-7413; bS. Ling, Z. Qi, D. P. Knight, Z. Shao, X. Chen, *Polym. Chem.* **2013**, *4*, 5401-5406.

[32]   aX. Hu, D. Kaplan, P. Cebe, *Macromolecules* **2006**, *39*, 6161-6170; bB. D. Lawrence, F. Omenetto, K. Chui, D. L. Kaplan, *J. Mater. Sci.* **2008**, *43*, 6967-6985.

[33]   I. C. Um, H. Kweon, Y. H. Park, S. Hudson, *Int. J. Biol. Macromol.* **2001**, *29*, 91-97.

[34]   aP. Cebe, B. P. Partlow, D. L. Kaplan, A. Wurm, E. Zhuravlev, C. Schick, *Acta Biomaterialia* **2017**, *55*, 323-332; bM. J. Rodriguez, T. A. Dixon, E. Cohen, W. Huang, F. G. Omenetto, D. L. Kaplan, *Acta Biomater.* **2018**, *71*, 379-387; cQ. Lu, X. Hu, X. Wang, J. A. Kluge, S. Lu, P. Cebe, D. L. Kaplan, *Acta Biomater.* **2010**, *6*, 1380-1387.

[35]   A. B. Salunkhe, V. M. Khot, N. D. Thorat, M. R. Phadatare, C. I. Sathish, D. S. Dhawale, S. H. Pawar, *Appl. Surf. Sci.* **2013**, *264*, 598-604.

[36]   A. Motta, L. Fambri, C. Migliaresi, *Macromol. Chem. Phys.* **2002**, *203*, 1658-1665.

[37]   R. C. Kambale, P. A. Shaikh, C. H. Bhosale, K. Y. Rajpure, Y. D. Kolekar, *Smart Mater. Struct.* **2009**, *18*, 115028.

[38]   R. K. Panda, R. Muduli, S. K. Kar, D. Behera, *J. Alloys and Compd.* **2014**, *615*, 899-905.

[39]   P. Kumar, S. K. Sharma, M. Knobel, M. Singh, *J. Alloys and Compd.* **2010**, *508*, 115-118.

[40]   M. T. Rahman, M. Vargas, C. V. Ramana, *J. Alloys and Compd.* **2014**, *617*, 547-562.

[41]   H. Luo, X. Zhou, C. Ellingford, Y. Zhang, S. Chen, K. Zhou, D. Zhang, C. R. Bowen, C. Wan, *Chem. Soc. Rev.* **2019**, *48*, 4424-4465.

[42]   R. Taherian, in *Electrical Conductivity in Polymer-Based Composites* (Eds.: R. Taherian, A. Kausar), William Andrew Publishing, **2019**, pp. 91-130.

[43]   K. Srinivasa Rao, S. V. Ranga Nayakulu, M. Chaitanya Varma, G. S. V. R. K. Choudary, K. H. Rao, *J. Magn. Magn. Mater.* **2018**, *451*, 602-608.

[44]   M. Stingaciu, H. L. Andersen, C. Granados-Miralles, A. Mamakhel, M. Christensen, *CrystEngComm* **2017**, *19*, 3986-3996.

[45]   aP. Martins, A. Lasheras, J. Gutierrez, J. M. Barandiaran, I. Orue, S. Lanceros-Mendez, *J. Phys. D: Appl. Phys.* **2011**, *44*, 495303; bM. Khan, A. Mumtaz, K. Hasanain, A. Ceylan, *Synthesis and Magnetic Properties of Cobalt Ferrite (CoFe2O4) Nanoparticles Prepared by Wet Chemical Route, Vol. 308*, **2006**; cG. D. Prasanna, H. S. Jayanna, A. R. Lamani, S. Dash, *Synth. Met.* **2011**, *161*, 2306-2311.

[46]   S. Chakraverty, M. Bandyopadhyay, *J. Phys.: Condens. Matter* **2007**, *19*, 216201.

[47]   M. M. Selvi, P. Manimuthu, K. S. Kumar, C. Venkateswaran, *J. Magn. Magn. Mater.* **2014**, *369*, 155-161.

[48]   D. Pal, M. Mandal, A. Chaudhuri, B. Das, D. Sarkar, K. Mandal, *J. Appl. Phys.* **2010**, *108*, 124317.
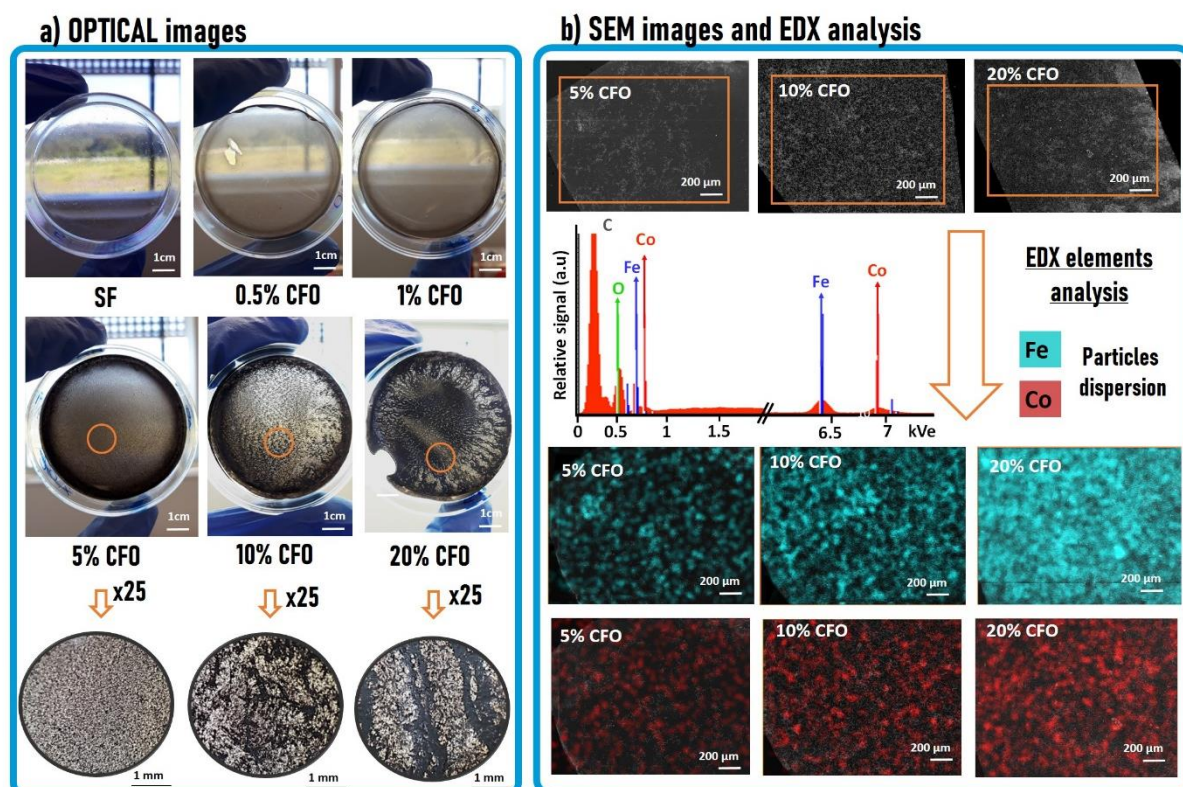
Figure 1. a) Optical images of SF/CFO films for 5 wt%, 10 wt% and 20 wt% CFO, b) SEM (above) and EDX (below) images of Fe (blue) and Co (red) for 5 wt%, 10 wt% and 20 wt% CFO samples.
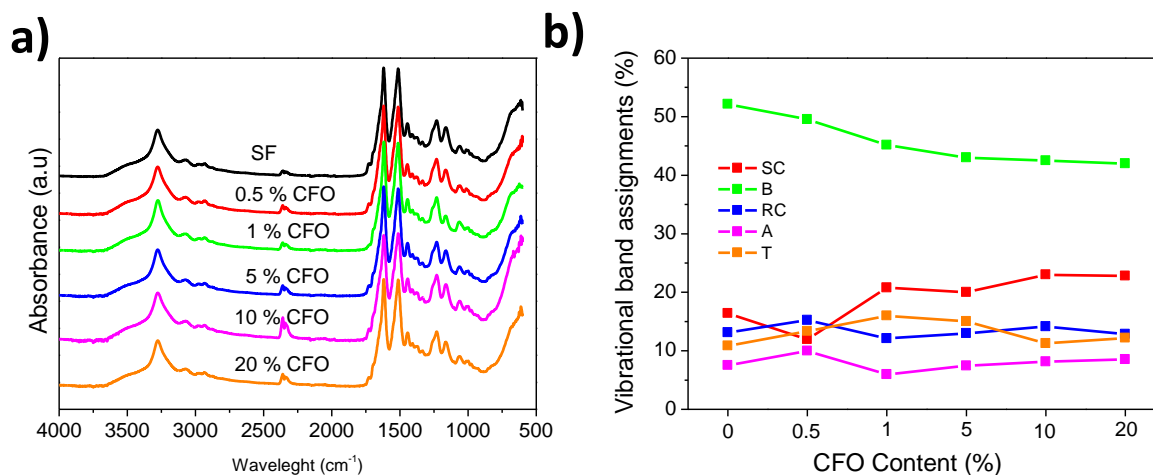

Figure 2. a) FTIR-ATR absorbance spectra and b) vibrational band assignment for side chains (SC), β-sheets (B), random coil (RC), α-helix (A) and turns (T) of CFO/SF nanocomposites.
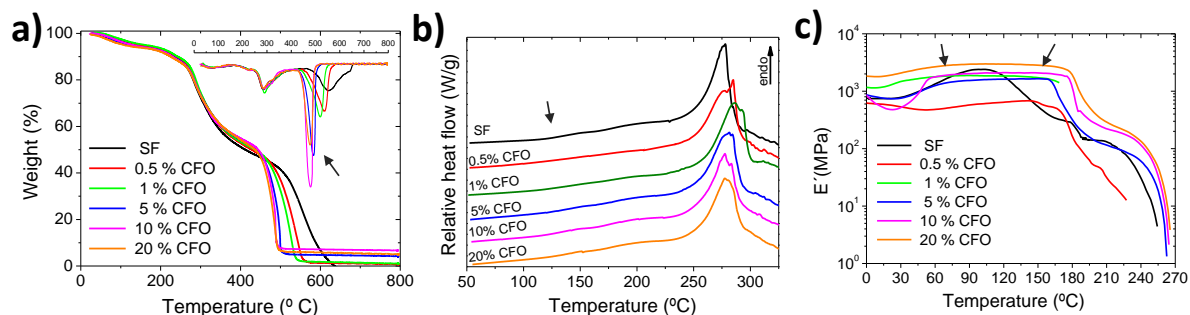
Figure 3. SF and CFO/SF nanocomposites: a) TGA and DTG thermogravimetric curves, b) DSC thermograms and c) storage modulus (E´) obtained after DMA measurements.
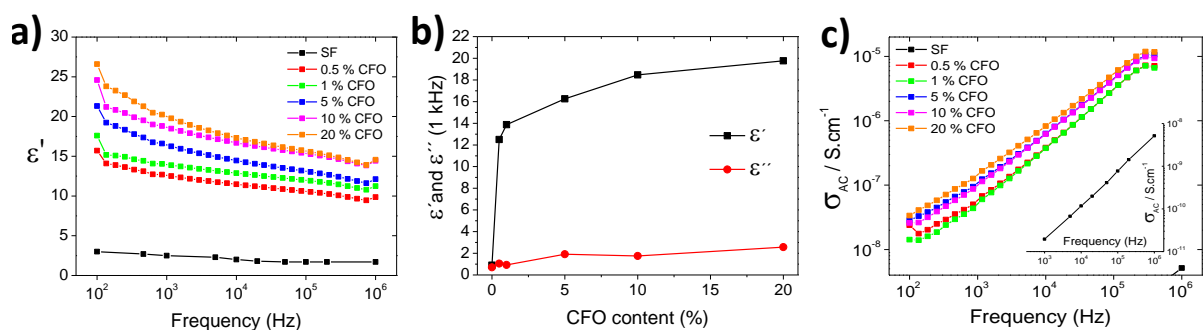

Figure 4. Dielectric constant, a) real (ε´) part, b) variation of the dielectric and imaginary (ε´´) constant as a function of CFO content at 1 kHz, c) a.c. electrical conductivity of the different CFO/SF nanocomposites.
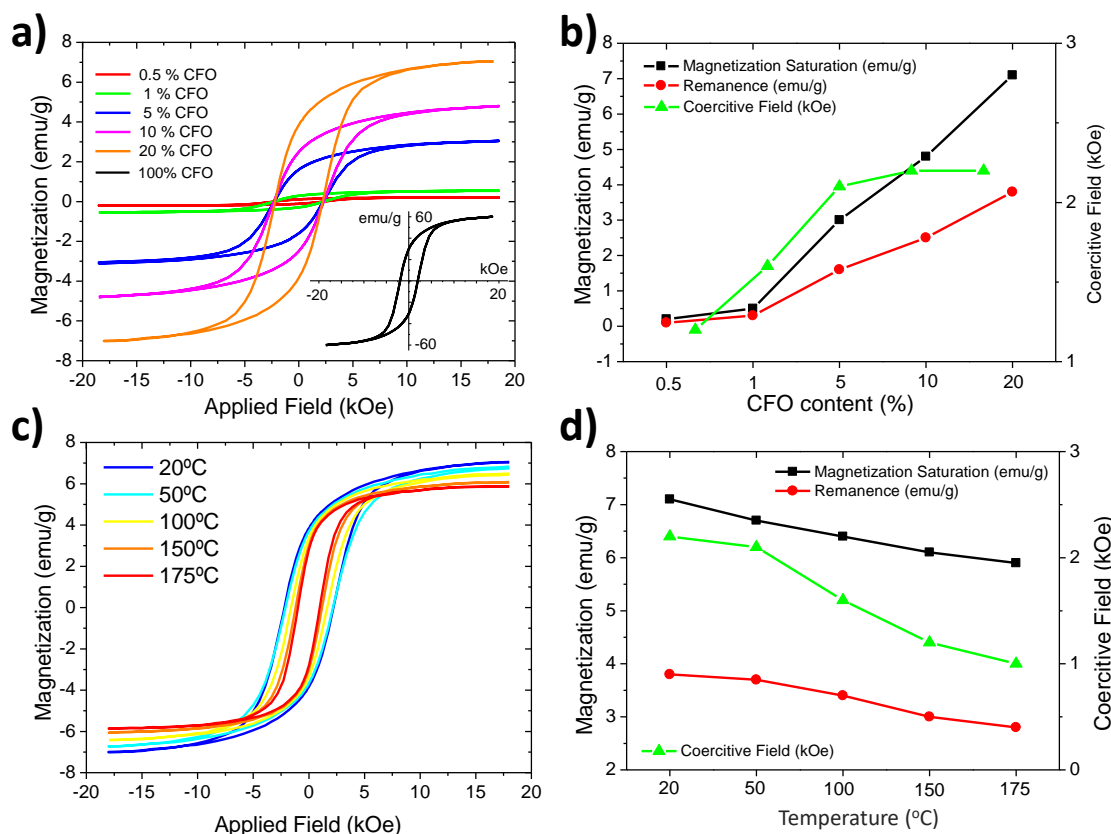
23

Figure 5. a) Room temperature hysteresis loops for neat CFO particles and CFO/SF nanocomposites b) magnetic properties of CFO/SF nanocomposites obtained from Fig. 5a, c) hysteresis loops measured at different temperatures for the 20 wt% CFO sample and d) temperature dependence of the magnetic properties for the 20 wt% CFO content sample.
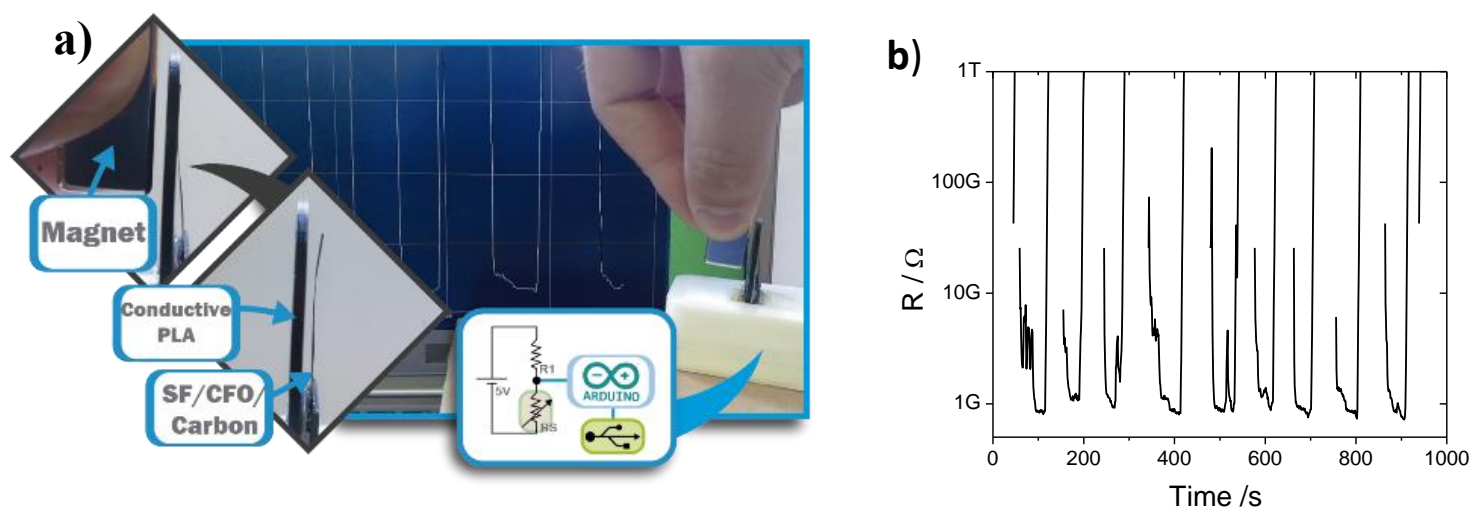

Figure 6. a) Electronic circuit and representation of the actuation by the magnet and b) Resistance variation as a function of time with the approximation of the magnet.
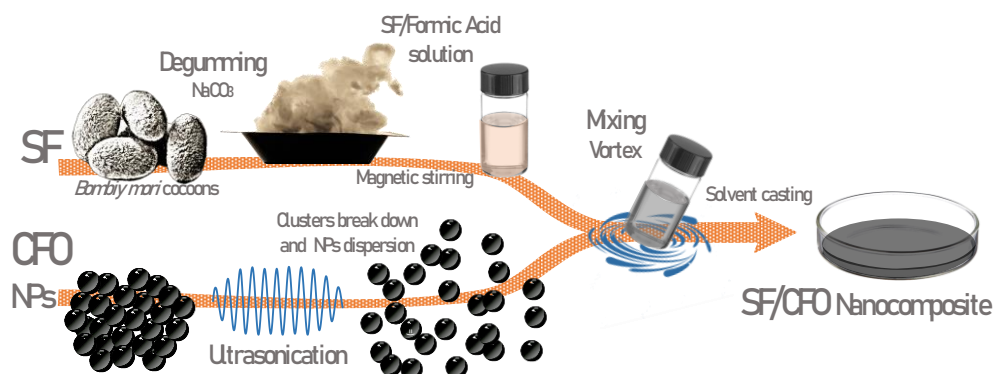
Figure 7. Schematic representation of SF/CFO films preparation.

Table 1. FTIR-ATR main absorption peaks of CFO/SF nanocomposites.

Bands (cm^{-1})	Assignments	Ref.
3500-3000	OH stretching vibration, H-bond and NH stretching vibration	[31]
1600-1700	**Amide I** (C=O stretching vibration, NH in plane bending, out of plane CN stretching vibration, and C-CN deformation)	
1517-1539	**Amide II** (stretching of C–N and N–H in-plane bending)	
1230	Amide III	
Amide I deconvolution peaks	**Assignments**	**Ref.**
1605–1615	Side chains	[32]
1619–1628/ 1697–1703	β-sheet crystal conformation	
1638–1655	Random coil	
1656–1662	α-helix	

WILEY-VCH

In order to minimize the environmental impact of technology, there is an increasing interest in developing advanced materials based on natural resources, reducing the actual dependence on fossil fuels. This work reports on magnetic nanocomposites based on Silk Fibroin (SF) polymer with magnetic $CoFe_2O_4$ (CFO) nanoparticles. Together with the discussion of the physico-chemical aspects of the composite as a function of filler concentration, the suitability of the materials for electronic applications has been demonstrated though the development of a magnetic actuator.

silk fibroin, magnetic nanoparticles, nanocomposite, magnetic actuator, smart and multifunctional materials

A. Reizabal[1,2], C.M. Costa[3,4*], N. Pereira[3,5], L. Perez[1,2], J.L. Vilas[1,2], S. Lanceros-Méndez[1,6*]

Silk fibroin based magnetic nanocomposites for actuator applications

ToC figure